High-power and high-temperature THz quantum-cascade lasers based on lens-coupled metal–metal waveguides

Alan Wei Min Lee,[1,*] Qi Qin,[1] Sushil Kumar,[1] Benjamin S. Williams,[1,2] Qing Hu,[1] and John L. Reno[3]

[1]*Massachusetts Institute of Technology, Cambridge, Massachusetts 02139, USA*
[2]*Currently with the University of California at Los Angeles, Los Angeles, California 90095, USA*
[3]*Sandia National Laboratories, Department 1123, MS 0601, Albuquerque, New Mexico 87185-0601, USA*
[*]*Corresponding author: awmlee@mit.edu*

Received June 8, 2007; revised August 11, 2007; accepted August 12, 2007;
posted August 29, 2007 (Doc. ID 83961); published September 25, 2007

A metal–metal waveguide quantum cascade laser with an abutted silicon hyperhemispherical lens is demonstrated at ~4.1 THz. The device produced 145 mW of peak pulsed power at 5 K with a wall-plug power efficiency of 0.7%, lasing up to a maximum operating temperature of 160 K. The far-field beam pattern has a full width at half-maximum value of ~4.8° in the H plane. The same device produced ~26 mW of peak power using a Winston cone instead of a lens, lasing up to 165 K. The large increase in output power is mainly attributed to an increase in collection efficiency. © 2007 Optical Society of America

OCIS codes: 140.3070, 140.0140.

Terahertz quantum-cascade lasers span 1.2 to 4.9 THz [1–3] and have potential uses as local oscillators [4] and as sources for illuminating focal-plane arrays in real-time imaging [5]. Thus far, the desirable high power levels (248 mW, pulsed [6]) and narrow beam patterns (11°, full width at half-maximum, FWHM [4]) have been obtained from quantum-cascade lasers using semi-insulating surface plasmon (SISP) ridge waveguides, a result of their spatially extended transverse mode profile (confinement factor $\Gamma \approx 0.1-0.5$). This produces a low-divergence beam as well as a low-reflectivity ($R \approx 0.32$) output facet, making mirror losses α_m comparable with waveguide losses α_w, resulting in high slope efficiencies, $dL/dI \propto \alpha_m/(\alpha_m+\alpha_w)$ [7]. However, based on the resonant-phonon design, our results show that these benefits result in a trade-off with higher threshold current densities (J_{th}) caused by greater waveguide losses, likely due to the large fraction of the mode in the nominally semi-insulating substrate, where impurity absorption could be significant. Due to these additional losses, operation of SISP devices is limited to temperatures below 105 K [6].

In comparison, metal–metal (MM) waveguides have a near unity confinement factor ($\Gamma \approx 1$) due to the highly confined mode propagating between the two metal strips; this essentially eliminates the additional loss from substrate absorption. The subwavelength confinement results in divergent beam patterns exceeding 120° and enhanced reflectivity at the end facets ($R \approx 0.7-0.9$, $\alpha_m \approx 0.5-2\ \mathrm{cm}^{-1}$) [7–9]. The additional reflectivity is due to a modal mismatch between the confined surface plasmon mode (attached to the closely spaced metal strips) and the near-field modes at the aperture, resulting in lower J_{th} and high maximum operating temperatures (T_{max}) of 169 K [10,11]. However, since α_m is small compared with α_w, these devices typically have lower slope efficiencies and power levels of tens of milliwatts. A strategy to increase α_m with minimal impact on T_{max} is to pattern a second-order distributed feedback grating in the top metal strip for surface emission [12,13]. These devices improve measured slope efficiency by reducing beam divergence in the grating axis, improving collection efficiency (η_{col}), resulting in ~10 mW power levels and single-mode operation. Alternately, a Fabry–Perot MM waveguide with a dielectric lens (Fig. 1) can be used to improve the beam pattern. In this work, silicon ($n_{Si} \sim 3.4$)—which is nearly index matched to the GaAs/AlGaAs active region ($n_{GaAs} \sim 3.6$)—is placed in contact with the output facet to increase η_{col}. The enhancement results from increased radiation in the forward direction due to the presence of the dielectric [14]. Analogously, slot antennas on dielectric substrates radiate power into air and the substrate in the ratio $1:\epsilon_r^{3/2}$ [14]. While the MM waveguide is not identical to a slot antenna, similar enhancements in directivity are expected in the patterns observed in [8,9]. Further enhancement is obtained by increasing the beam directivity with the lens. This approach leads to higher powers and better beam patterns without significantly reducing T_{max}, in contrast with SISP devices.

The device is based on the resonant-phonon depopulation design and uses the same active region

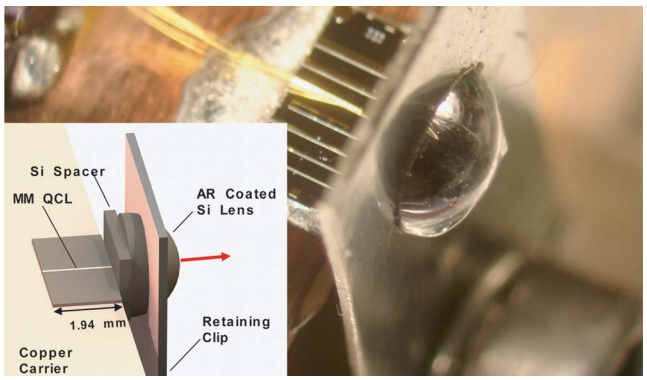

Fig. 1. (Color online) Metal–metal THz quantum-cascade laser (QCL) with abutted HRSi spacer and lens.

described in [6]. The MM waveguide was fabricated using the wet-etching processing described in [12], with the waveguide oriented so that the facets could be defined by cleaving. An ~80 μm wide by 1.94 mm long device was aligned and indium soldered to a copper carrier so that the output facet was flush with the carrier edge, allowing a double-side-polished, 340 μm thick, high-resistivity silicon (HRSi, >10 KΩ cm) spacer to be epoxied to the carrier and remain in contact with the facet. Close positioning of the spacer was critically important, with similarly sized devices producing <100 mW, likely due to gaps between the facet and the spacer. The fixed spacer provided a mating surface for the HRSi lens, preventing damage to the facet during lens alignment. The lens has a 3 mm diameter and a total length of 1.62 mm, making the total setback from the center 0.46 mm, roughly at the R/n aplanatic point [14]. To reduce reflections at the lens surface, the lens was antireflection (AR) coated using a ~14 μm thick layer of low-density polyethylene (LDPE, $n \approx 1.5$) which acts as a quarter-wave matching layer at the lasing frequency of 4.1 THz. In a separate measurement, a single side of a flat HRSi wafer was coated with this film, improving transmission by ~30% (from 49% to 63% through the wafer). A transmission of ~90% is then deduced for the Si/LDPE/air interface ($0.9 \approx 1.3 \times 0.7$, where 70% is the transmission of the Si/air interface). The lens was positioned against the spacer and held in contact by a spring steel retaining clip. The position of the lens with respect to the facet was aligned at room temperature by dissipating heat pulses in the device and imaging the facet onto an infrared microbolometer camera operating in differential mode [5]. This allowed fine alignment of the lens with respect to the laser facet, prior to cryogenic laser operation.

The device was mounted in a vacuum cryostat with a polypropylene window and biased with 200 ns pulses repeated at 50 kHz for a total duty cycle of 1%. The output power was measured versus current (Fig. 2) using a pyroelectric detector, with the peak power calibrated with a thermopile powermeter (ScienTech model AC2500H). At 5 K, $J_{th} = 266$ A/cm^2 with a maximum peak power of 145 mW lasing up to 160 K. The slope efficiency was $dL/dI = 296$ mW/A near threshold and was 140 mW/A at the peak, with a maximum wall-plug power efficiency of 0.7%. For comparison with an open facet, the lens and spacer were removed and the device was tested using a Winston cone to collect the emitted power. At 5 K, $J_{th} = 254$ A/cm^2 with a peak power of 26 mW, lasing up to 165 K. Due to a thermal runaway problem of the MM devices fabricated from this wafer, several devices failed catastrophically in CW operation [11]. As a result, all pulsed measurements (with and without the lens) were concluded before attempting CW measurements. After remounting the spacer and lens, the device produced a peak power of 102 mW with 2 μs long pulses at 25% duty cycle before failing. This failure was not associated with the lens setup. Similar lens-coupled MM devices fabricated from a different wafer (FL179C-M9-2, lasing at ~2.7 THz) yielded ~50 mW of CW power.

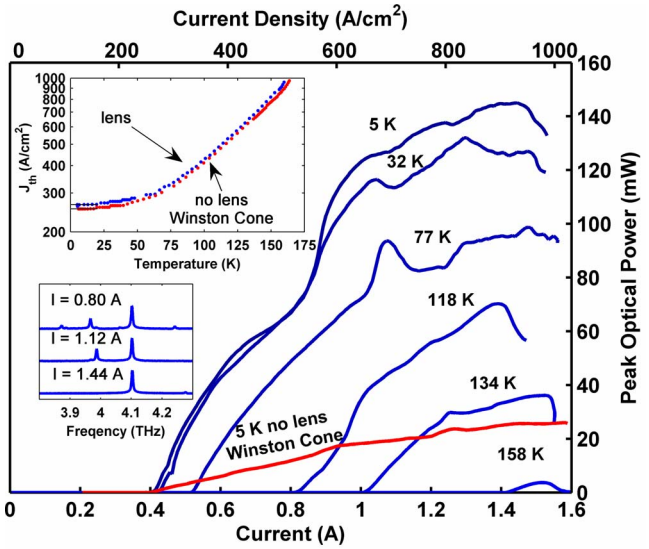

Fig. 2. (Color online) Light versus current: lens-coupled and Winston cone-coupled devices. Insets: top, J_{th} versus temperature; bottom, typical spectra of the device with a lens.

An expression for the measured slope efficiency is $\eta_{col} \cdot \alpha_m/(\alpha_m + \alpha_w)$, with the observed change in slope efficiency (5.5×) resulting from increases in η_{col} or α_m. The small difference in J_{th} and T_{max} suggests a small increase in α_m since J_{th} should increase with $(\alpha_m + \alpha_w)$. However, deduction of α_m is hampered by the unknown transparency current and hence the gain-current relation in the resonant-phonon gain medium, as a parasitic current channel below the designed bias sets the transparency current density at substantially different than zero [15]. A larger influence is expected from improved η_{col}, which is estimated numerically for bare-faceted and lens-coupled devices (Fig. 3). A full-wave simulation is used to determine the far-field patterns for the front and rear facets of the bare and lens-covered devices. For the lens-coupled device an HRSi half-space is assumed for the front facet covering, as the lens/air boundary is $\sim 70\lambda_{Si}$ from the facet. A superposition of the front and rear far-field patterns (in the forward direction) separated by the device length is then used to model the far-field pattern of the device. Collection efficiency is determined using the collection angle of the bare facet, which is ~15° limited by the aperture of the powermeter (29 mm diameter, 55 mm from the device). For the lens-coupled facet the collection angle is $\beta_{max} = \sin^{-1}(r \cdot \sin(\gamma)/sb) \sim 70°$ (set back, sb = 0.46 mm) limited by critical angle (γ) at the lens/air boundary, which is unaffected by the AR coating. Though this beam pattern model is simpler than the one in [9], when it was applied at the wavelengths and device dimensions of [8] the interference fringe separation agreed with the measured patterns. This analysis precludes the use of a Winston cone because the cone is optically close ($\sim 3.5\lambda_o \sim 250$ μm) to the front facet, making the use of far-field ray tracing unjustified. Moreover, the entrance aperture of the Win-

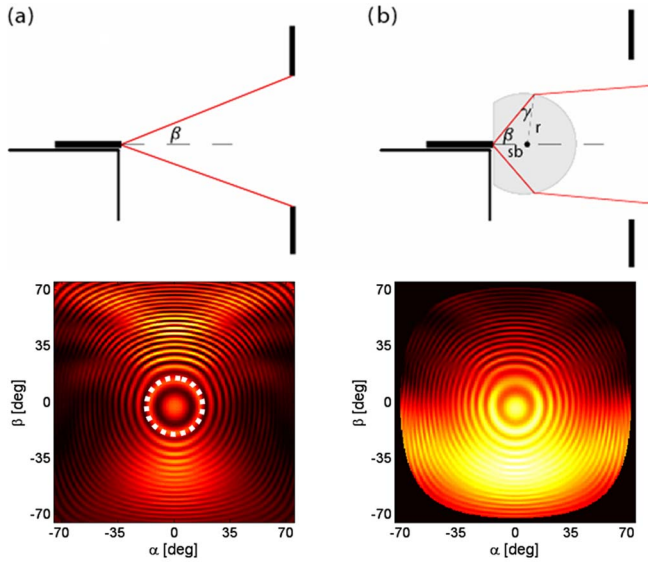

β_{max}	η_{col} – Mode 0	η_{col} – Mode 2	η_{col} – Mode 4
15°	3.5% (16×)	2.5% (22×)	2.1% (23×)

Fig. 3. (Color online) Top row, collection angle (β): (a) bare facet, (b) lens-coupled. Middle row, calculated beam pattern: bare facet [(a), collected power circled], lens-coupled [(b) into HRSi, uncollected power blackened]. Bottom row, collection efficiency of the bare facet for even lateral modes; the expected relative improvement of the lens-coupled facet is shown in brackets.

ston cone is computationally large $\sim 26\lambda_0$ (1.9 mm), preventing a three-dimensional full-wave simulation. However, the relative improvement in η_{col} of the Winston cone over the bare facet is determined experimentally to be 4.3×, which allows a comparison of Winston cone and lens-coupled configurations. For the fundamental lateral mode (mode 0), $\eta_{col} \approx 3.5\%$ for the bare facet and reduces slightly for higher-order lateral modes due to increasing divergence. The lens greatly enhances forward radiation (i.e., it improves directivity), results in a dramatically different beam pattern, $\eta_{col} \approx 62\%$, and improves the slope efficiency by ~16×, including the transmission of the AR coating. Including the improvement of the lens on the Winston cone (5.5×), the overall lens to bare-facet improvement is ~23×, reasonably agreeing with the numerical results.

To verify the high directivity of the lens-coupled configuration, the FWHM of the beam was measured in the H plane using a rotation stage and a pyroelectric detector (12 mm aperture) placed 30 cm from the device. Both the far-field beam pattern and a cross section of the beam pattern from the microbolometer camera have a FWHM ≈ 4.8° (Fig. 4). Diffraction patterns in the beam image at 6 cm are likely due to spurious reflection; however these patterns disappeared in the far field. In conclusion, our work demonstrates that careful optical engineering of lens-coupled metal–metal waveguide THz lasers can produce high power levels with good beam patterns, while preserving their advantage of higher T_{max}.

This work is supported by the Air Force Office of Scientific Research, NASA, and the National Science Foundation. Sandia is a multiprogram laboratory operated by Sandia Corporation, a Lockheed Martin Company, for the United States Department of Energy under Contract DE-AC04-94AL85000.

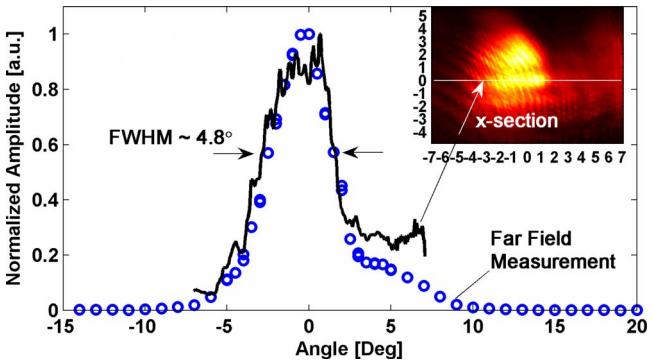

Fig. 4. (Color online) Far-field (30 cm) beam pattern (circles) and cross section of the beam image at 6 cm (inset, $I = 1.47$ A).

References

1. R. Köhler, A. Tredicucci, F. Beltram, H. E. Beere, E. H. Linfield, A. G. Davies, D. A. Ritchie, R. C. Iotti, and F. Rossi, Nature **417**, 156 (2002).
2. J. Faist, presented at the Optical Terahertz Science and Technology Topical Meeting, Orlando, Fla., USA, March 18–21, 2007.
3. Q. Hu, B. S. Williams, S. Kumar, A. W. M. Lee, Q. Qin, J. L. Reno, H. C. Liu, and Z. R. Wasilewski, *Future Trends in Microelectronics*, S. Luryi, J. M. Xu, and A. Zaslavsky, eds. (Wiley, 2007), pp. 347–358.
4. H. W. Hübers, S. G. Pavlov, A. D. Semenov, R. Köhler, L. Mahler, A. Tredicucci, H. E. Beere, D. A. Ritchie, and E. H. Linfield, Opt. Express **13**, 5890 (2005).
5. A. W. M. Lee, B. S. Williams, S. Kumar, Q. Hu, and J. L. Reno, IEEE Photon. Technol. Lett. **18**, 1415 (2006).
6. B. S. Williams, S. Kumar, Q. Hu, and J. L. Reno, Electron. Lett. **42**, 89 (2006).
7. S. Kohen, B. S. Williams, and Q. Hu, J. Appl. Phys. **97**, 053106 (2005).
8. A. J. L. Adam, I. Kašalynas, J. N. Hovenier, T. O. Klaassen, J. R. Gao, E. E. Orlova, B. S. Williams, S. Kumar, Q. Hu, and J. L. Reno, Appl. Phys. Lett. **88**, 151105 (2006).
9. E. E. Orlova, J. N. Hovenier, T. O. Klassen, I. Kašalynas, A. J. L. Adam, J. R. Gao, T. M. Klapwijk, B. S. Williams, S. Kumar, Q. Hu, and J. L. Reno, Phys. Rev. Lett. **96**, 173904 (2006).
10. B. S. Williams, S. Kumar, Q. Hu, and J. L. Reno, Opt. Express **13**, 3331 (2005).
11. S. Kumar, "Development of terahertz quantum-cascade lasers," Ph.D. dissertation (Massachusetts Institute of Technology, to be published in 2007).
12. S. Kumar, B. S. Williams, Q. Qin, A. W. M. Lee, Q. Hu, and J. L. Reno, Opt. Express **15**, 113 (2007).
13. J. A. Fan, M. A. Belkin, F. Capasso, S. Khanna, M. Lachab, A. G. Davies, and E. H. Linfield, Opt. Express **14**, 11672 (2006).
14. D. B. Rutledge, D. P. Neikirk, and D. P. Kasilingam, in *Infrared and Millimeter-Waves* Vol. 10, K. J. Button, ed. (Academic, 1983), pp. 1–90.
15. H. Callebaut, S. Kumar, B. S. Williams, Q. Hu, and J. L. Reno, Appl. Phys. Lett. **83**, 207 (2003).